# CHAPTER IV

## Effect of shell precursor concentration on optical and photocatalytic properties of core-shell $TiO_2$-$SnO_2$ nanostructures

In the previous chapter, we have discussed about various temperature dependant properties of $TiO_2$ nanoparticles along with three core-shells where the core was annealed at different temperature. We also went on a detailed survey of optical properties of MgO nanostructures which acted as the shell in case of the core-shell structures. By comparing the individual properties of core and shell along with the core-shell nanostructure, we found no trace of shell characteristics in the hybrid structure. This may be attributed to the almost insulating band gap of MgO which is around 7.8 eV. So this time we attempted with a shell layer of $SnO_2$ which has a band gap 3.7 eV almost near to the band gap of the core $TiO_2$ i.e 3.2 eV (in bulk). So, in this chapter we shall absorb ourselves in quenching the following queries

- Will a coating with a material of near band gap energy significantly affect the core properties?
- What will be the influence on the optical and photocatalytic properties of the core when the shell concentration is varied? Will it attain a saturation level at certain extent?

In this chapter, we have undergone a detailed analytical and qualitative study over the optical properties of core $TiO_2$ nanostructures when it is coated with three different shell concentrations. The structural and morphological properties are studied with the help of XRD pattern, TEM images, Raman, XPS and EDX spectra. The samples were characterized for the optical perspective through UV-vis absorbance spectra, PL spectra and TRPL analysis. Also the photoactivity of all the samples under day light was studied to achieve degradation of methylene blue.

## 4.1 Synthesis of core-shell $TiO_2$-$SnO_2$ nanostructures

Core $TiO_2$ nanoparticles are prepared via a simple sol-gel method as we have already discussed in *chapter III*. $SnO_2$ nanoparticles were synthesized following [1] only with an increment of the pH to 11. The synthesis of $SnO_2$ nanoparticles is started with the addition of 1 gm of $SnCl_2.2H_2O$ in a mixture of 11 ml deionized water and 5 ml of ethanol and is allowed to stir for 5 min. Then 1 ml HCl is added drop wise to the above solution. After stirring it for 15 min the solution is fixed at pH 11 by drop wise addition of aq. ammonia. By this procedure, $SnO_2$ solutions of three different

concentrations were prepared namely 0.2 M,0.4 M and 0.6 M. This solution is stirred for 2–3 h at 80° C. To the prepared $TiO_2$ nanoparticles, $SnO_2$ solutions were added dropwise followed by stirring for 4-5 hours then centrifuging and drying at 80° C to obtain the three core-shell $TiO_2$-$SnO_2$ nanostructures named as TS2,TS4 and TS6.

## 4.2 Structural and morphological characterizations

### 4.2.1 XRD pattern analysis

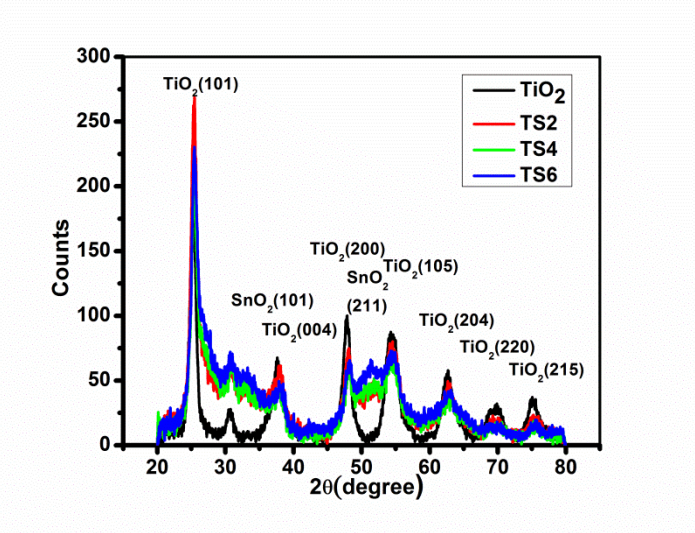


Fig. 4.1: XRD pattern of core $TiO_2$ along with core-shell $TiO_2$/$SnO_2$ nanostructures with different shell concentrations

Fig. 4.1 shows the XRD patterns of $TiO_2$ and its corresponding core-shells TS2, TS4 and TS6. From the figure, it is clearly predictable that the core $TiO_2$ nanoparticles possess all the anatase peaks along with a low intensity brookite peak around $2\theta = 32^{\circ}$. The diffraction peaks of $TiO_2$ for different values of $2\theta$= (25,38,48,54,63,69,75) from different crystal planes {(101),(004),(200),(105),(204),(220),(215)} respectively are found in the pristine $TiO_2$ nanoparticles as well as all the three core-shell structures. Also two peaks of $SnO_2$ are found in the core-shell nanostructures indicating its presence in the core-shell sample. It is very clear from the image that with increase in $SnO_2$ concentration, the intensity of shell related peaks are enhanced e.g TS6 exhibits highest intensity peak at $SnO_2$ (211). Alternately highest intense peak at $TiO_2$ (101) is found at TS2 confirming sufficient concentration of $TiO_2$ in the sample.

We have determined the lattice strain of each sample using Williamson-Hall (*W-H*) equation (described in *chapter 2 section 2.2.1*). We have calculated the microstrain and crystallite sizes of all the core-shell nanostructures along with core $TiO_2$ which are presented in table 4.1.

Table 4.1: Calculation of microstrain and crystallite size

| Sample name | Crystallite size (nm) | Microstrain |
|---|---|---|
| $TiO_2$ | 8 | 0.0053 |
| TS2 | 10 | 0.00275 |
| TS4 | 11 | 0.0175 |
| TS6 | 12 | 0.00436 |

When the size of a material is reduced from bulk to nano, lots of surface defects occur in the particle owing to the high surface to volume ratio present in the nanocrystal. We can see that the strain is significantly decreased in the core-shell structure with lowest shell concentration. When the core is coated with an external shell layer, the system comes under an external compressive strain. Compressive force imparts a negative strain in the system. But, in case of core-shell structures, the oxygen vacancy related defects play a vital role in increasing the strain. That is why the strain is reduced but it does not come to negative value although a bit lessened than the strain of the core structure. However with increase in shell concentration, the shell material is under high tensile strain due to coherent growth on the core structure. This further increases the strain in TS4. Also the lattice mismatch between $TiO_2$ and $SnO_2$ plays a vital role enhancing the microstrain in TS4. In the earlier case, we can see from XRD pattern that TS2 exhibits almost all characteristic peaks of $TiO_2$ due presence of very thin coating layer of $SnO_2$. But the lattice mismatch increases with increase in shell concentration as we can see that with increasing shell concentration, the $SnO_2$ related peaks have become more intense. However for the constant core size, growth of a larger shell exceeds the critical thickness for accommodation of electron and can only be accommodated by the formation of defects that relax the strain between core and shell. Therefore the sample TS6 is showing negligible strain [2]

Also the calculation of crystallite sizes for each sample indicates that with increase in shell concentration, the crystallite sizes are also increased. This is because of the fact that coating the core material enhances the crystallinity of the core-shell system because the shell is not amorphous in the sample. So, with increasing shell thickness, it is accompanied with increasing crystalline size because the crystallite size of the shell also takes part in enhancing the crystallite size of the whole system [3].

### 4.2.2 HRTEM image analysis

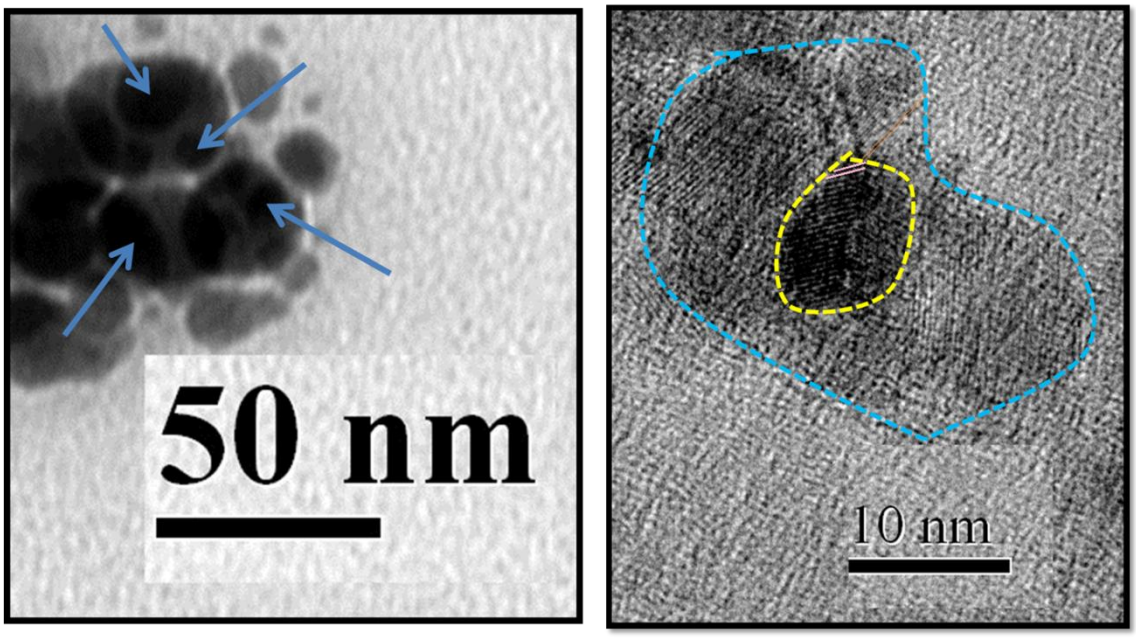


Fig. 4.2: Low resolution (left) and High resolution (right) TEM image of $TiO_2$-$SnO_2$ nanostructures

Fig. 4.2 (left) shows the low resolution tem image of core-shell $TiO_2$-$SnO_2$ nanostructures. The blue colored arrows indicate the core portion in the surrounding shell layer. One shell seems to accommodate more than one core nanoparticle [3]. Agglomeration is present in the sample as we did not use any kind of surfactant while synthesizing the sample. From the HRTEM image (Fig. 4.2, right) the core size is found to be 8 nm whilst the shell size is estimated as 10 nm in average. We have to measure the average thickness of the shell as the shell layer is not uniform surrounding the core. The core lattice planes are indicated by pink colored lines while the shell planes are indicated with orange colored lines.

### 4.2.3 EDX spectra nanlysis

The EDX pattern further confirms the presence of all constituent elements in the core-shell structure which is shown in Fig 4.3.

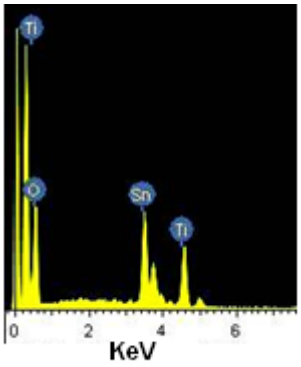


Fig. 4.3: EDX spectra of core-shell $TiO_2$-$SnO_2$ nanostructures

### 4.2.4 Raman spectra analysis

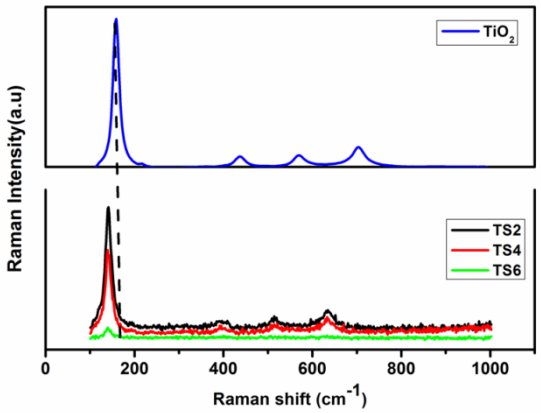


Fig. 4.4 Raman spectra of the core $TiO_2$ and the synthesized core-shell (TS2, TS4 and TS6)

Fig 4.4 shows the Raman spectra for core $TiO_2$ and the three core-shell nanostructures TS2, TS4 and TS6. In case of $TiO_2$, an intense Eg peak has appeared at 144 $cm^{-1}$, followed by low intense A1g, B1g peaks at 410 $cm^{-1}$, 520 $cm^{-1}$ and at 630 $cm^{-1}$ respectively [4-5]. The 144 $cm^{-1}$ peak occurs prominently in core $TiO_2$ which is red shifted to 140 $cm^{-1}$ in case of all the core-shell nanostructures. The intensity of the peaks are found to be decreasing w.r.t the core and also found to be suppressed with

increasing shell thickness where in TS6 all the peaks except the $E_g$ peak vanish permanently.

The size of the nanocrystals, presence of defects have a profound effect on the Raman peak position, line width, etc. To study the effect of size, defects and temperature on the position, width of the Raman peak, we have considered the Eg Raman peak. Xu et al. [6] used a phonon confinement model to explain the observed changes in the Raman line and position using Heisenberg uncertainty principle.

$$\Delta X\, \Delta P \geq \hbar/2 \quad \ldots\ldots\ldots\ldots\ldots\ldots\ldots\ldots (4.1)$$

Where $\Delta X$ is crystallite size, $\Delta P$ is the phonon momentum distribution and $\hbar$ is reduced Planck constant. When it comes to a perfect crystal, first order Raman scattering of photons abide by the phonon selection rule $q$=0, implying phonon contribution at the center of Brillouin zone. Thus, when $\Delta X$ increases as we can see in our case, $\Delta P$ decreases resulting in very less amount of phonon contribution. This leads to shifting as well as contraction of the active Raman peak. The red Raman downshifts are mainly accredited to either size-induced phonon confinement [7] or lattice defects, such as point defects, dislocations and stacking faults [7]. Again the strength of a bond is determined by its force constant and the force constant of a bond is associated with frequency by $\upsilon \infty \sqrt{k}$ [8]. The increase in oxygen vacancies in the core-shell nanostructure plays a vital role in red shifting of the Raman peak as number of Ti-O bonds decrease due to lack of oxygen atoms hereby decreasing the force constant and the wave number also thus gets reduced.

The shell acts as a shield for the phonons to interact more thus decreasing the Raman intensity. The disappearance of Raman bands for the core-shell nanostructure TS6 indicates that $TiO_2$ nanostructure is completely surrounded by a shell of sufficient thickness , which does not allow much optical phonon of $TiO_2$ (core) to participate in the Raman scattering process[11].

Table 4.2: Calculation of bond width of active raman peak and phonon lifetime

| Sample name | $E_g$ bond width ($cm^{-1}$) | Phonon lifetime (pico sec) |
|---|---|---|
| $TiO_2$ | 15.45 | 0.3 |
| TS2 | 16.68 | 0.89 |
| TS4 | 16.66 | 0.9 |
| TS6 | 15.31 | 1.08 |

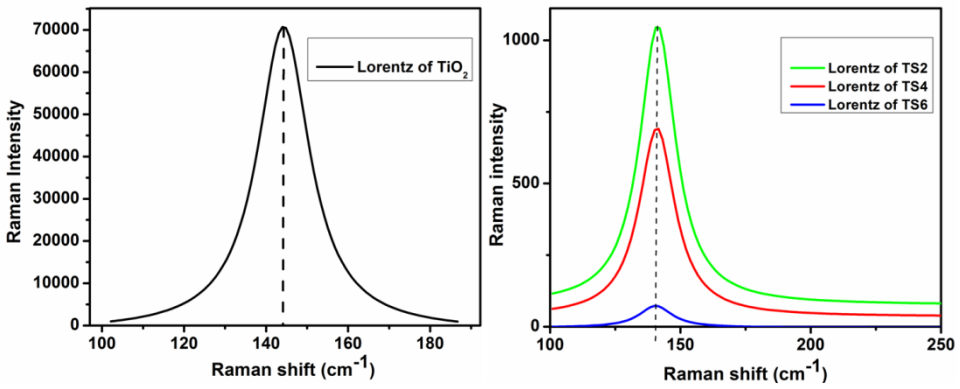


Fig. 4.5: $E_g$ bond vibration of core $TiO_2$ and the synthesized core-shell (TS2, TS4 and TS6)

We have calculated the phonon lifetime, considering Eg mode, in each sample by adopting the energy-time uncertainty relation, $\Delta E/\hbar = 1/\tau = 2\pi c\Gamma$, where $\Delta E$ is uncertainty in the energy of phonon mode, $\hbar$ is reduced plank constant, $\Gamma$ is the FWHM of the Raman peak [9]. The calculated phonon lifetimes are tabulated in table 4.2. It is obvious from the table that the phonon lifetime increases in case of the core-shell nanostructures. As we can see from Table 4.1 that crystallite size of all the core-shell nanostructures are much higher than that of $TiO_2$ and this leads to an increase in the phonon density hereby increasing the anharmonic phonon coupling. This finally enhances the decay time or the lifetime of the phonons [9]. The line width broadening is caused by size distribution of $TiO_2$ NCs and phonon confinement effect in the $TiO_2$ NCs [10]. The enhanced Raman line bond width is due to the presence of lattice defects which occurred as a result of lattice mismatch between the core and shell. So although in TS2, the Raman line width has increased a lot but it again goes on

decreasing order with increase in shell thickness which may be attributed to the fact that the Raman line width is inversely proportional to the size of the nanocrystals.

### 4.2.5 XPS spectra analysis

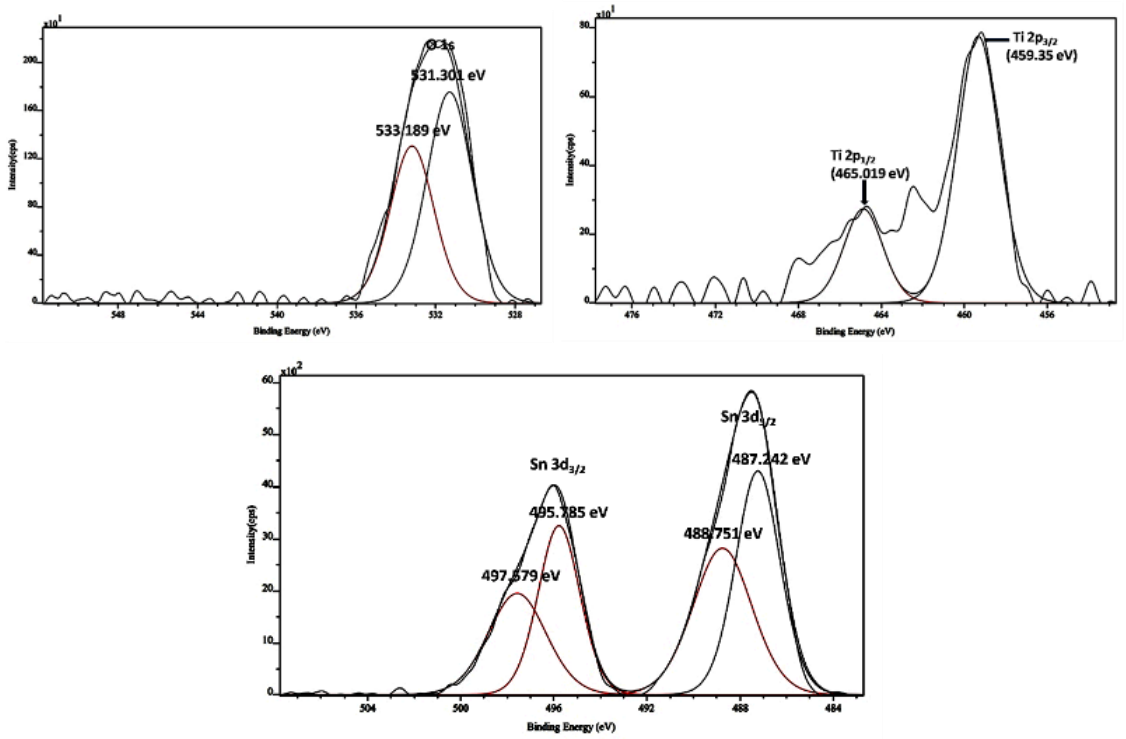


Fig. 4.6 XPS spectra of core-shell $TiO_2$-$SnO_2$ nanocrystal

Fig 4.6 shows the XPS spectra of core-shell $TiO_2$-$SnO_2$ nanostructures. The XPS spectra of pristine $TiO_2$ has already been analysed in the earlier chapter (section 3.6.6). So, here we can see that in the core-shell structure, the $O_L$ peak is shifted to 531.301 eV whilst the $O_H$ peak shifts to 533.189 eV. Both $O_L$ and $O_H$ peaks move to higher binding energies and this shift may be attributed to $TiO_2$-x or $SnO_{2-y}$ after addition of $SnO_2$ to $TiO_2$ [3]. While analyzing the Sn spectra in the core-shell structure, it is found that Sn $3d_{5/2}$ and Sn $3d_{3/2}$ peaks are present in the core-shell nanostructure but both of them are de convoluted as doublets. Sn $3d_{5/2}$ is found at two positions (487.242 eV, 488.751 eV) whereas Sn $3d_{3/2}$ is obtained at two positions (495.785 eV, 497.579 eV). The higher binding energy related peaks correspond to $Sn^{4+}$ state while the lower binding energy related peaks are attributed to $Sn^{2+}$ state. The occurrence of the $Sn^{2+}$ state in the core-shell structure indicates the presence of oxygen vacancy in the sample

[12]. This result demonstrates that $Sn^{4+}$ ions close to oxygen vacancies inhabit two electrons from the oxygen vacancy cavity Vo and transform to $Sn^{2+}$ ions yielding an F center. Actually, when an O atom is lost from the $SnO_2$ lattice , the electron pair that remains trapped in the vacancy cavity Vo leaves behind a pair of electrons which give rise to an F center.The basic assumption is that the two electrons in F centre tend to occupy the neighboring $Sn^{4+}$ion and yield $Sn^{2+}$ center[12].

$V0+2e^- = F$……eqn (4.2)

$Sn^{4+} + 2e^- = Sn^{2+}$……eqn(4.3)

The XPS analysis of Ti shows that it is in $^{4+}$ state. Again, it is seen in the core-shell nanostructures that, the Ti $2p_{3/2}$ peak (458.6 eV) is shifted to higher binding energy (459.350 eV) .The same goes for $Ti2p_{1/2}$ peak (464.8 eV) which is shifted to 465.019 eV

## 4.3 Optical Property analysis

Core $TiO_2$ and all the three core-shells TS2, TS4 and TS6 were characterized to realize their optical properties and how they change w.r.t that of the core/

### 4.3.1 UV-vis absorbance spectra analysis

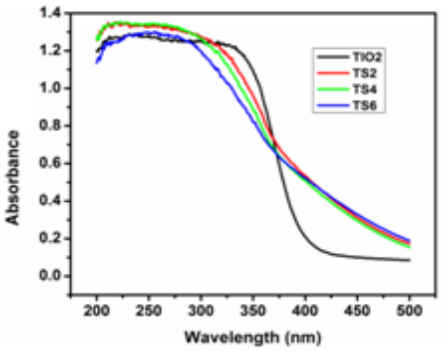


Fig. 4.7: Absorbance spectra of core $TiO_2$ and core-shell (TS2, TS4 and TS6) nanostructures

Fig 4.7 reveals the UV-vis absorbance spectra of core $TiO_2$ along with the three core-shell nanostructures. $TiO_2$ has shown sharp UV absorbance with two peaks at ~225 nm and 330 nm. The 225 nm peak of $TiO_2$ is seen all the three core-shells. But a surprising

phenomenon is observed as unlike other core-shell nanostructures, the 330 nm peak position is blue shifted in the core-shell nanostructures and this shift is more prominent with increasing shell thickness. It is observed that TS6 is behaving completely like the shell $SnO_2$ as the later is also found to exhibits absorbance peak around 290 nm. So a coupling mechanism might have occurred between the core and shell where a few of the UV photons excited are absorbed by the outer shell and may be due to high shell thickness, the excitation source does not have enough intensity to penetrate the shell. Thus the absorbance features of the core are being suppressed resulting in distinct characteristics resembling the shell. But it can be clearly seen that the absorbance intensity of the core-shell nanostructures in the visible regime is enhanced far more than the core structure which is an essential condition for the applicability of the material. The absorption hump of $TiO_2$ in the visible region may be due to $Ti^{3+}$ defect related states as well as oxygen vacancies present in the sample. The same goes for the core-shell structures which may occur due to $Sn^{2+}$ states as well as increment of oxygen vacancies in the core-shell structures.

The Urbach energy is calculated by plotting the *lnF(R)* vs. E and are shown in Fig. 4.8. The absorption is calculated by Kubelka-Munk plot. The band gap of the nanomaterials were calculated from a plot of the modified Kubelka-Munk function $[F(R)E]^{1/2}$ vs the energy of absorbed light E The calculated Urbach energy values and the band gap values are tabulated below in Table 4.3.

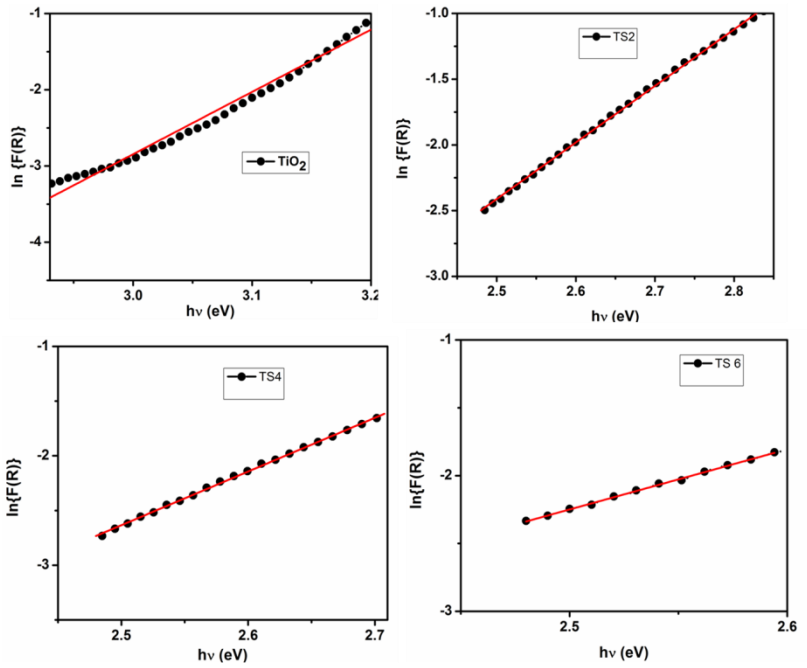


Fig. 4.8: Urbach energy plot of core $TiO_2$ and core-shell (TS2, TS4 and TS6) nanostructures

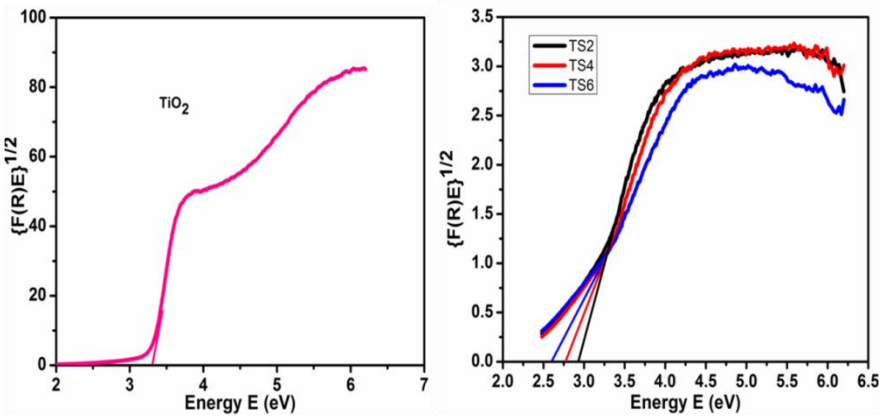


Fig. 4.9: Tauc's Plot for of core $TiO_2$ and core-shell (TS2, TS4 and TS6) nanostructures

Table 4.3: Calculation of urbach energy and band gap

| Sample name | Urbach energy (meV) | Band gap (eV) |
|---|---|---|
| $TiO_2$ | 122 | 3.25 |
| TS2 | 232 | 2.9 |
| TS4 | 204 | 2.75 |
| TS6 | 225 | 2.6 |

From table 4.3 we can find that there is remarkable increase in Urbach energy when $TiO_2$ nanoparticles are annealed and are coated with $SnO_2$ shell layer. It is well established that the growth of the shell leads to prominent strain and formation of defect states at the core/shell interface or within the shell [13]. These can serve as trap centres for photogenerated charge carriers. The excited electrons are captured by the shallow defect bands, preventing their direct transition to the conduction band hereby increasing the Urbach energy to such high extent. But as we increase the shell thickness which consequently results in decreasing the band gap; implying that for a constant core, the valance band position of the shell will move upwards while the conduction band position will shift downwards. So, in the shell the distance between the valence band and conduction band becomes very low and hence there is lot more probability of recombination of electrons and holes in the sample. Thus some of the electrons are lost instead of getting trapped in defect centers reducing the Urbach energy. But still the urbach energy is higher than that of the core $TiO_2$ as due to formation of core-shell structure, charge separation is still more than in the core. The charge separation is schematically shown in Fig. 4.12. Again as we have explained in paragraph (strain), when the shell thickness overcomes a critical thickness, it becomes unable to accommodate the electrons and the electrons tend to stay in various defect related trap sites which further increases the Urbach energy.

### 4.3.2 Photoluminescence spectra analysis

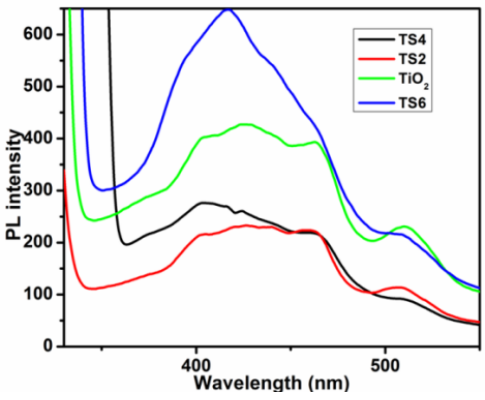


Fig. 4.10: Comparative room temperature PL spectra of core $TiO_2$ and core-shell (TS2, TS4 and TS6) nanostructures, excited at a wavelength of 350 nm

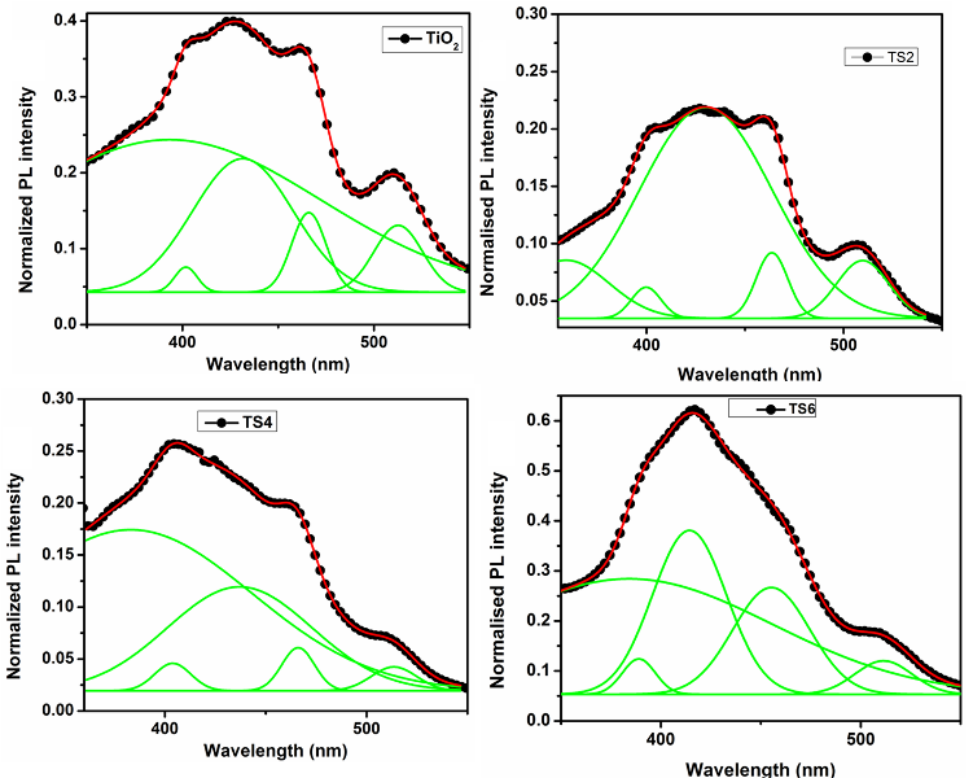


Fig. 4.11: Gaussian fit of PL spectra of core $TiO_2$ and core-shell (TS2, TS4 and TS6) nanostructures

Fig 4.10 shows the PL of core $TiO_2$ as well as all the three core-shell $TiO_2$-$SnO_2$ nanostructures. This figure is plotted as a comparative diagram to show that in case of TS2 and TS4, the luminescence intensity is suppressed than that of the core $TiO_2$. This is resembling TYPE 2 core-shell structure as due to enhanced charge separation in the core-shell structure, there is less probability of overlapping of electrons and holes in the core-shell structure which is schematically shown in Fig.4.12.

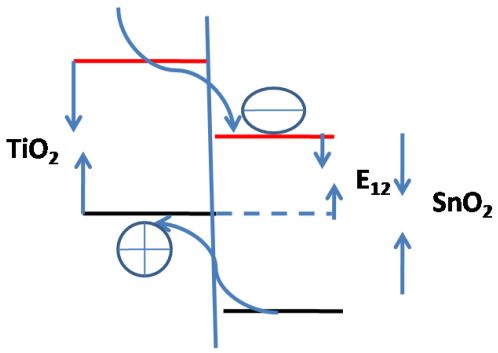


Fig. 4.12: Charge separation in core-shell $TiO_2$-$SnO_2$

Fig 4.11 displays the Gaussian fitting of the PL intensities of all the core-shell nanostructures along with the core counterpart to realize the exact positions of the PL peak. We can see that core and all three core-shells exhibit an emission peak at 390 nm. This peak is due to phonon assisted indirect transition from $M \rightarrow \Gamma$ in the Brillouin zone. But it is prominent that the intensity of the peak is suppressed in the core-shell nanostructure TS2 and TS4. This is due to the fact theat the outer $SnO_2$ shell that is covering the core $TiO_2$ nanoparticles. The lowering of the $TiO_2$ related UV peak should be due to relatively thick and dense MgO layer, thus the excitation source does not have enough penetration intensity to excite the inner $TiO_2$ nanoparticles. Again, the photo-generated charge carriers emitted from the $TiO_2$ core get absorbed by the $TiO_2$ NPs which are formed on the surface of the core [14].

Although the photo-generated charge carrier emission from the $TiO_2$ core is very strong, the $TiO_2$ NPs which are developed on the surface of $TiO_2$ core can absorb some of the emission, ensuing decrease of the UV emission [14].Also from the charge separation diagram we can see that both electron and hole are spatially separated at the interface of the core and shell due to their band alignments. The visible emission peaks are associated with excitons, oxygen vacancies and different surface defect states [15-17]. $TiO_2$, TS2 and TS4 exhibit an intense emission peak around 425 nm which is assigned to self trapped exciton (STE) recombination [18-19]. But an anomaly has occurred in TS6 sample as the PL intensity of 390 nm peak has enhanced along with occurrence of another peak at 380 nm. This may be due to the fact that with utmost shell thickness, the lattice mismatch between the core and shell increases to a higher extent resulting in occurrence of the additional peak while destructing the STE peak completely.

### 4.3.3 TRPL spectra analysis

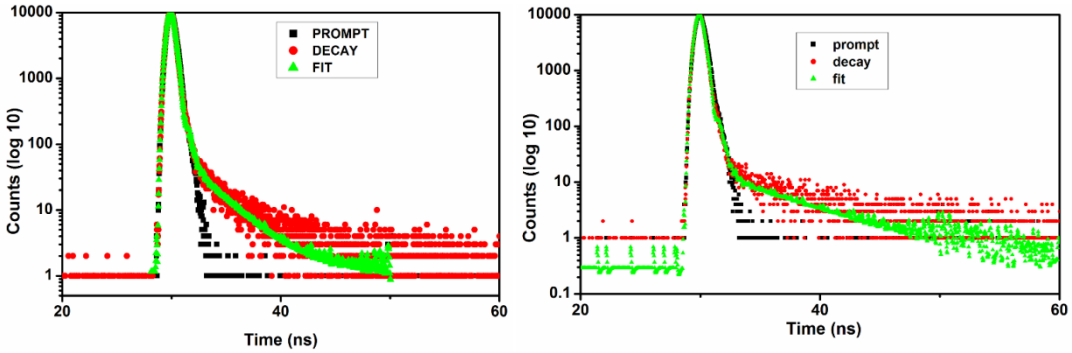


Fig. 4.13: TRPL spectra of (left) core $TiO_2$ and (right) core-shell $TiO_2$-$SnO_2$

Fig. 4.13 shows the TRPL spectrum for both core $TiO_2$ and core-shell $TiO_2$-$SnO_2$ nanostructures. A four exponential was fitted to calculate the life time of $TiO_2$ whilst a five exponential was needed to find out the same for $TiO_2$-$SnO_2$ through the following equation

$$y = y_0 + \sum_{i=1}^{n} \alpha_I \exp(-t/\tau_i) \ldots\ldots \text{(for n exponential)}$$

From the graph, the values of $\tau_1 = 5.052403E \times 10^{-12}$sec, $\tau_2 = 6.115959 \times 10^{-11}$sec, $\tau_3 = 5.526903 \times 10^{-11}$sec and $\tau_4 = 2.843263 \times 10^{-9}$sec. The values of $\alpha_1$ = -219.0319, $\alpha_2$ = -13.22373, $\alpha_3$= 16.22717and $\alpha_4 = 2.337827\times10^{-4}$

The lifetime of core-shell $TiO_2$-$SnO_2$ is found to be 8.04 pico sec which is calculated using the parameters $\tau_1 = 4.828623 \times 10^{-11}$sec, $\tau_2 = 5.827831 \times 10^{-11}$sec, $\tau_3 = 5.689869 \times 10^{-11}$sec, $\tau_4 = 6.183882 \times 10^{-9}$sec and $\alpha_1$ = -57.02612,$\alpha_2$= -319.5732, $\alpha_3$ = 376.1231 and $\alpha_4 = 4.546176\times10^{-5}$. The lifetime of electron in the core-shell structure is found to be 0.015 nano sec which is much more higher than that of the core structure that is 0.005 nano sec indicating that there is very less recombination in the sample. This once again stands with the TYPE 2 structure of core-shell $TiO_2$-$SnO_2$. The spatial separation of electron and hole leads to reduced wave function overlap and thus longer lifetime of charge recombination is expected in TYPE 2 heterostructures. Our observation indicates that the formation of shell leads to an increase in lifetime, which can be concluded as the clear evidence of reduced electron hole wave function overlap in core-shell material. Upon coating, the number of oxygen vacancies increases (also found in XPS spectra), and therefore large number of carriers

are trapped in these defect centers. Thus, as compared to the pristine one, the electrons in the coated system now can transit from one defect related state to another state and then to the valence band until they find emission center. The oxygen vacancies, with trapped electrons, act as charged defects. Therefore, these charged oxygen vacancies can also interact with the mobile electrons and scatter them, thereby decreasing their mobility [20]. Decrease in mobility results in separation of the electrons-holes for longer time resulting in increase in the lifetime.

## 4.4 Application of core $TiO_2$ nanoparticles and core-shell $TiO_2$-$SnO_2$ nanostructures in photocatalysis

Photocatalytic activities of pure $TiO_2$ nanoparticles and core-shell $TiO_2$-$SnO_2$ nanostructures were examined by observing the degradation of methylene blue (MB) under daylight. The photoactivity was studied under daylight lamp of 500 watt power Xenon lamp in the wavelength range from 400-700 nm as described in earlier chapters. The decrease of concentration or degradation of methylene blue from its initial concentration was studied by observing the decrease of the absorption peak ($A_t$) of the dye solution irradiated for the aforementioned period. The degradation efficiency of phenol solution is given by $\{(A_0-A_t)/A_0\}\times100\%$ [21] where $A_0$ is the initial concentration of the dye solution. The rate constants were determined using $1^{st}$ order reaction kinetics as mentioned in chapter 2 (section 2.3.3)

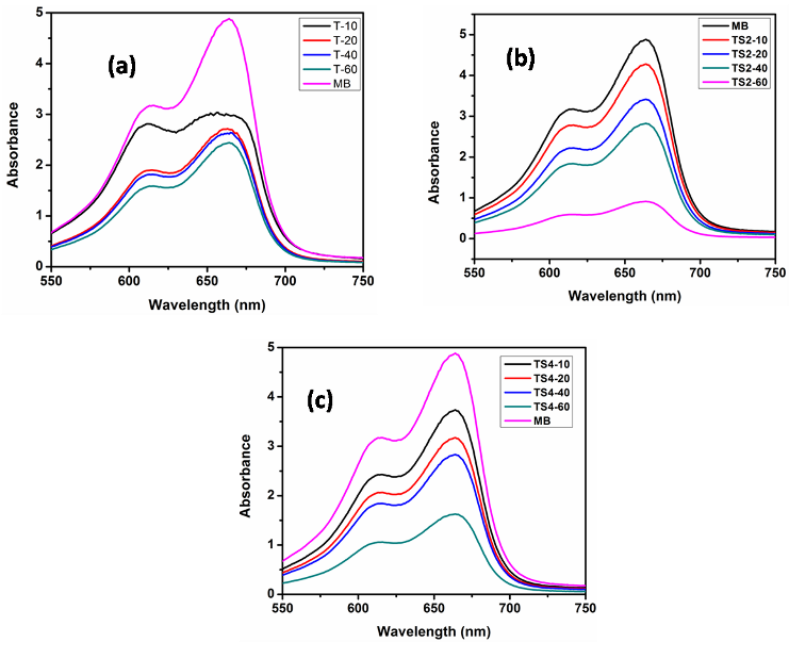


Fig. 4.14: Absorbance of MB in presence of catalyst (a) $TiO_2$, (b ) TS2 and (c) TS4

Fig. 4.14 shows the photocatalytic degradation scenario of core $TiO_2$ and TS2, TS4 core-shell nanostructures. The degradation efficiencies and rate constants are tabulated in table 4.4.

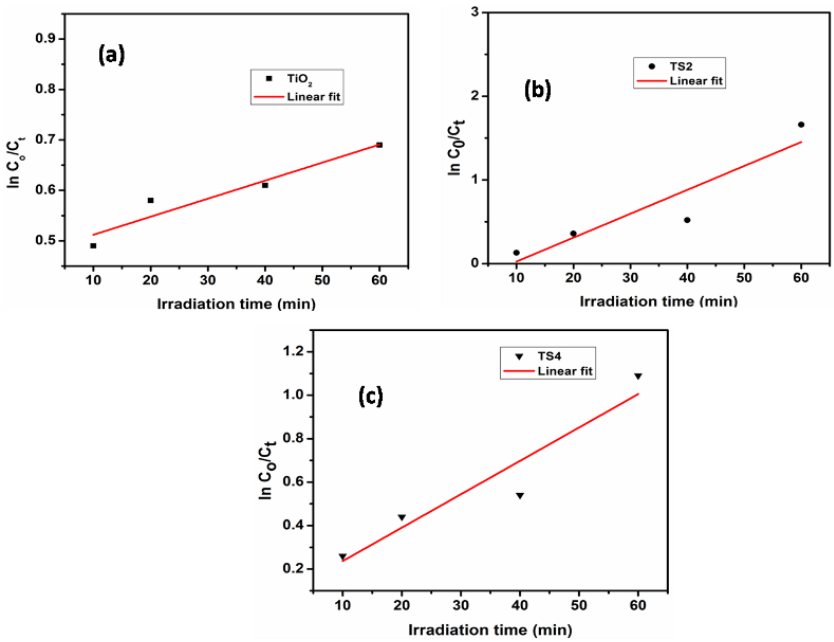


Fig. 4.15: ln $C_o/C_t$ vs irradiation time graph for determination of rate constant

Table 4.4: Calculation of rate constant and degradation efficiency

| Sample name | Rate const ($min^{-1}$) | % degradation w.r.t time of irradiation | | | |
|---|---|---|---|---|---|
| | | 10 min | 20 min | 40 min | 60 min |
| $TiO_2$ | 0.003 | 38.6 | 44 | 42.5 | 50.1 |
| TS2 | 0.02 | 12.11 | 29 | 42 | 81.66 |
| TS4 | 0.015 | 24.2 | 35.5 | 42 | 66.9 |

We can see that the highest degradation efficiency obtained for $TiO_2$ to degrade methylene blue (MB) is 50.1%. The core shell structures TS2 and TS4 exhibited very high degradation efficiencies when irradiated for 60 min. Also from the calculation of rate constants it is found that the core-shell nanostructures are far better photocatalytic agent than the core counterpart. A possible mechanism for degradation of MB was demonstrated in an earlier report by considering work functions of MB (5.67 eV), excited MB (3.81 eV), conduction band of $TiO_2$ (4.25 eV) and the conduction band of $SnO_2$ (4.5 eV) [22] while similar mechanism for photodegradation of RhB has been proposed by Zhang et al [23]. MB excited in the presence of daylight can efficiently transfer electrons into the $TiO_2$ conduction band. The slow degradation of MB by $TiO_2$ is attributed to the electron recombination between the injected electron and surface adsorbed MB (holes) (arrow in Fig. 4.16). But the scenario is different for the $TiO_2$/$SnO_2$ core-shell system where electrons first jump into the $TiO_2$ conduction band and then can be transferred to the conduction band of $SnO_2$. This leads to prominent separation between the electron and hole by increasing their lifetime (mentioned in section 4.3.3). The electron in the conduction band of $SnO_2$ can then be trapped by dissolved oxygen to form reactive oxygen species which then degrade the dye MB. The MB molecules adsorbed directly onto $SnO_2$ nanoparticles can transfer electrons into the conduction band of $SnO_2$, which in turn leads to the degradation of MB via the same process described above.

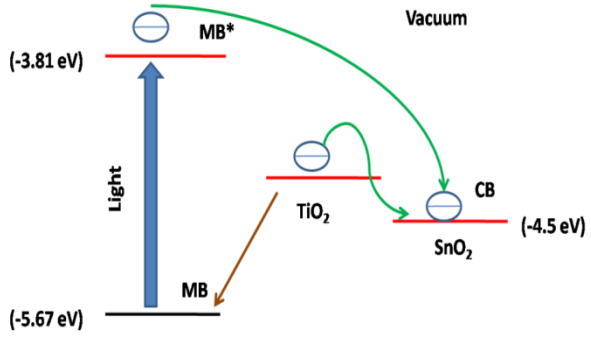


Fig. 4.16: Charge transfer schematic diagram

But we could not find any degradation for TS6 sample. There was an indication in the PL spectra that the nanostructure may not be applicable as a photocatalyst due to highly intense luminescence. This may be because of the fact that charge separation is very low in the sample and also maximum number of electrons are lost in recombination. Another reason may be the following fact that, with the shell thickness so high, the light source does not have enough energy to excite the inner core electrons and those electrons which are excited they could not tunnel to the surface of the material to take part in the reaction that yields degradation of MB molecules on the surface.

## 4.5 Conclusion

Thus in this chapter we have made a clear effort to answer the questions which were the aim to work on this material. We can see that coating $TiO_2$ with a near band gap material like $SnO_2$ significantly affected its properties specially in case of UV-vis absorbance spectra where we could see the core-shell structure was behaving entirely like the shell material. Again with increase in shell thickness, enhancement of properties was observed until we obtained a shell thickness which exceeded the critical thickness for accommodating the electron the shell conduction band. Thus we failed to obtain any significant contribution from TS6 sample but TS2 and TS4 have established themselves to be excellent photocatalytic agents than performed far better than core $TiO_2$ in degrading both phenol as well as MB.

## References

[1] Basyach. P., et al. Enhanced Photocatalytic Activity of Core-Shell $TiO_2$/$SnO_2$ Nanostructures under UV Illumination, *IJSER* **4**(12), 28--31, 2013.

[2] Smith, A.M., et al. Tuning the Optical and Electronic Properties of Colloidal Nanocrystals by Lattice Strain, *Nat Nanotechnol*. **4**(1), 56--63, 2009.

[3] Chetri, P., et al. Exploring the structural and magnetic properties of $TiO_2$/$SnO_2$ core/shell nanocomposite: An experimental and density functional study, *J. Solid State Chem.***220**, 124--131, 2014.

[4] Brojcin, M.G., et al. Infrared study of laser synthesized anatase $TiO_2$ nanopowders, *J. Phys. D: Appl. Phys.* **38** (9), 1415--1420, 2005.

[5] Zhang, W.F., et al. Raman scattering study of anatase $TiO_2$ nanocrystals, *J. Phys. D: Appl. Phys.* **33** (8), 912--916, 2000.

[6] Xu, C.Y., et al. Blue shift of Raman peak from coated $TiO_2$ nanoparticles, *J. Raman Spectrosc.* **32** (10), 862--865, 2001.

[7] Nie, A., et al. Epitaxial $TiO_2$/$SnO_2$core–shell heterostructure by atomic layer deposition, *J. Mater. Chem.* **22**, 10665--10667, 2012.

[8] Brojcin, M.G., et al. Infrared study of laser synthesized anatase $TiO_2$ nanopowders, *J. Phys. D: Appl. Phys.* **38** (9), 1415--1420, 2005.

[9] Zhang, J., et al. UV Raman spectroscopic study on $TiO_2$:I: Phase transformation at the surface and in the bulk , *J. Phys. Chem. B.* **110** (2), 927--935, 2006.

[10] Giri, P. K., & Dhara, S., Freestanding Ge/$GeO_2$ Core-Shell Nanocrystals with Varying Sizes and Shell Thicknesses: Microstructure and Photoluminescence Studies, *J. Nanomater.* **2012**, 905178--905183, 2012.

[11] Kumar, S., et al. Synthesis and Raman signature for the formation of CdO/$MnO_2$ (core/shell) nanostructures, *J. Raman Spectrosc.* **45**, 717--722, 2014.

[12] Santara, B., et al. Evidence of oxygen vacancy induced room temperature ferromagnetism in solvothermally synthesized undoped $TiO_2$ nanoribbons, *Nanoscale* **5**, 5476--5488, 2013.

[13] Reiss et al, Core/Shell Semiconductor Nanocrystals**,** *Small* **5**(2)**,** 154--168,2009.

[14] Sookhakianan , M., et al. Synthesis, structural, and optical properties of type-II ZnO–ZnS core–shell nanostructure, *J. Lumin.* **145**, 244--252, 2014.

[15] Tang, H., et al. Photoluminescence in TiO2 anatase single crystals, *Solid State commun.* **87** (9), 847--850, 1993.

[16] Yamada, Y., & Kanemitsu, Y. Blue photoluminescence of highly photoexcited rutile TiO2: Nearly degenerate conduction-band effects, *Phys. Rev. B.* **82** (11), 113103, 2010

[17] Preclikova, J., et al. Nanocrystalline titanium dioxide films: Influence of ambientconditions on surface- and volume-related photoluminescence, *J. Appl. Phys.* **108** (11), 113502, 2010.

[18] Liu, J., et al. Structure and photoluminescence study of TiO2 nanoneedle texture along vertically aligned carbon nanofibre arrays, *J. Phys. Chem. C.* **112** (44), 17127--17132, 2008.

[19] Yu, J., et al. Effects of F-doping on the photocatalytic and microstructure of nanocrystalline $TiO_2$ powders, *Chem. Mater.* **14** (9), 3808--3816, 2002.

[20] Wang, X., et al. Trap states and carrier dynamics of TiO2 studied by photoluminescence spectroscopy under weak excitation condition, *Phys. Chem. Chem. Phys.* **12** (26), 7083--7090, 2010.

[21] Choudhury, B., et al. Extending Photocatalytic Activity of $TiO_2$ Nanoparticles to Visible Region of Illumination by Doping of Cerium, *Photochem. Photobiol.* **88**, 257--264, 2012.

[22] Seema, H., et al. Graphene–SnO2 composites for highly efficient photocatalytic degradation of methylene blue under sunlight, *Nanotechnology* **23**, 355705(1--8), 2012.

[23] Zhang, J., et al. Graphene–metal–oxide composites for the degradation of dyes under visible light irradiation, *J. Mater. Chem.* **21** 3634--3640,2011.